Simulation of Aluminum Micro-mirrors for Space Applications at Cryogenic Temperatures

J.L. Kuhn*, S.B. Dutta**, M.A. Greenhouse***, and D.B. Mott**

* NASA Goddard Space Flight Center, Code 542, Greenbelt, MD, USA
jonathan.kuhn@gsfc.nasa.gov
** NASA Goddard Space Flight Center, Code 553, Greenbelt, MD, USA
*** NASA Goddard Space Flight Center, Code 685, Greenbelt, MD, USA

ABSTRACT

Closed form and finite element models are developed to predict the device response of aluminum electrostatic torsion micro-mirrors fabricated on silicon substrate for space applications at operating temperatures of 30K. Initially, closed form expressions for electrostatic pressure and mechanical restoring torque are used to predict the pull-in and release voltages at room temperature. Subsequently, a detailed mechanical finite element model is developed to predict stresses and vertical beam deflection induced by the electrostatic and thermal loads. An incremental and iterative solution method is used in conjunction with the non-linear finite element model and closed form electrostatic equations to solve the coupled electro-thermo-mechanical problem. The simulation results are compared with experimental measurements at room temperature of fabricated micro-mirror devices.

Keywords: micro-mirrors, simulation, cryogenic, electrostatic, thermal.

1 INTRODUCTION

NASA Goddard Space Flight Center (GSFC) is developing two-dimensional tilt-able aluminum Micro-Mirror Arrays (MMA) for Earth and space science applications, such as actively controlled masks for spectrometers. Due to science requirements, each micro-mirror element must be a factor of six larger than the Digital Micro-mirror Devices (DMD) developed by Texas Instruments, while maintaining similar rotation angles, resulting in much larger gap distances for electrostatic actuation. In addition, these devices must operate at 30K, resulting in potentially severe thermal mismatch stresses.

Our objective is to enable optimal design of the GSFC MMA through detailed modeling and simulation of a single micro-mirror element shown in Fig. 1. In this work we present improved theoretical and finite element models to simulate the device response at ambient and cryogenic temperatures. In particular, a theoretical model similar to that presented in Ref. [1] is developed, but extended to account for large angles of rotation. Also, a finite element model is developed using shells instead of bricks for high aspect ratio members to more accurately account for the vertical deflection and stiffness of the torsion bars. The analytical and finite element results are compared with results from fabricated micro-mirrors.

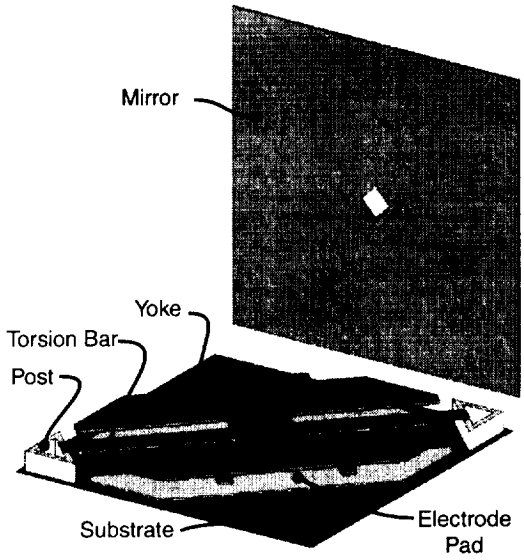

Figure 1: Single micro-mirror element.

2 ELECTRO-MECHANICAL SIMULATION

In this section we present approximate equations governing the electro-mechanical response of a micro-mirror element. These equations are developed neglecting the vertical deflection of the torsion bars. As a result, we also present a finite element model, which can be used to more accurately estimate local stresses.

The models are developed for the set of parameters shown in Fig. 2. In this figure the coordinate system is aligned with the torsion bars as shown. The torsion bar dimensions are length L_{bar}, width w_{bar}, and thickness t_{bar}. Three key points are labeled as a, b, and c. Their respective x locations are x_a, x_b, and x_c. The only y location needed in the simulation is y_b. Under an applied voltage the yoke rotates through angle θ about the y axis.

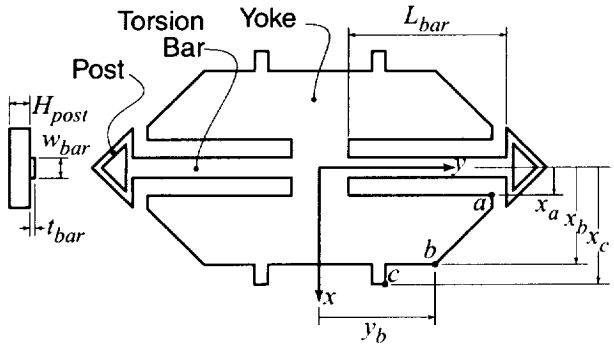

Figure 2: Post, torsion bar, and yoke geometry and parameters.

2.1 Analytical Model

The micro-mirror motion is driven by applying an electrostatic field between two plates offset from the torsion bar central axis. The two plates are non-parallel in general, and the electrostatic pressure distribution is non-uniform. The resulting pressure distribution, derived using the Laplace (Ref. [2] pg. 34) and Maxwell Stress Tensor (Ref. [2] pg. 261) equations, is

$$P_e(x,\theta) = \frac{\varepsilon_0 V^2}{2\rho(x,\theta)^2\theta^2} \tag{1}$$

where ε_0 is the permittivity of air, θ is the inclination angle, and $\rho(x,\theta)$, for the coordinate system shown in Fig. 2 is

$$\rho(x,\theta) = \left(\frac{d_0}{sin\theta} - \frac{x}{cos\theta}\right). \tag{2}$$

In the above equations, V is the applied voltage, d_0 is the initial distance between the two electrostatic plates, and x is the coordinate relative to the system shown in Fig. 2. These equations neglect electrostatic edge effects, but are not limited to small inclination angles. The total electrostatic torque is

$$T_e(V,\theta) = \int_{x_a}^{x_b}\int_{-Y(x)}^{Y(x)} xP_e(x)\,dy\,dx \tag{3}$$

where the edges of the yoke between points a and b are approximated by the line $Y(x) = x_b + y_b - x$. Equation (3) can be be expanded to

$$T_e(V,\theta) = \frac{\varepsilon_0 V^2}{\theta^2}\int_{x_a}^{x_b} \frac{xY(x)}{\rho(x,\theta)^2}\,dx \tag{4}$$

The reacting mechanical torque can be computed using beam equations. In this case the mechanical torque is

$$T_m(\theta) = 2\frac{\theta KG}{L_{bar}} \tag{5}$$

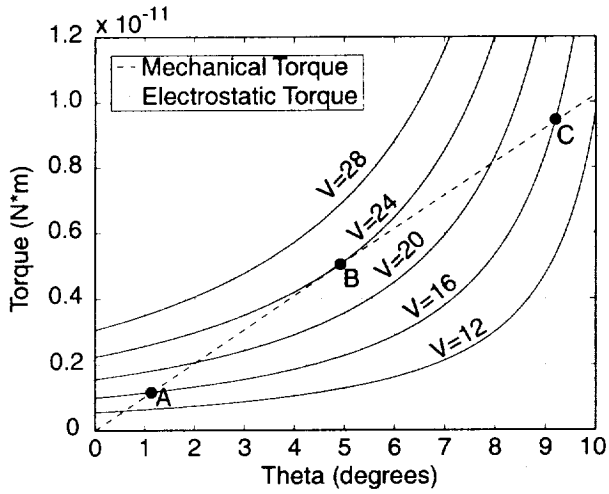

Figure 3: Electrostatic and mechanical torque versus yoke inclination angle.

where θ is the twisting angle and corresponds with the relative inclination angle θ between the yoke and electrode pad. The term G is the shear modulus, and L_{bar} is the length of one of the torsion beams. The factor of 2 accounts for both torsion beams. Finally, K is the torsional stiffness, which is [3]

$$K = ab^3\left[\frac{16}{3} - 3.36\frac{b}{a}\left(1 - \frac{b^4}{12a^4}\right)\right]. \tag{6}$$

The above equation is for a beam with solid rectangular section, of width $2a$ and thickness $2b$. In this case, $a = w_{bar}/2$, and $b = t_{bar}/2$. Equations (3) and (5) are plotted in Fig. 3, for $L_{bar} = 47.0\ \mu m$, $w_{bar} = 6.0\ \mu m$, $t_{bar} = 0.3\ \mu m$, $x_a = 12.7\ \mu m$, $x_b = 29.5\ \mu m$, $x_c = 35.5\ \mu m$, $y_b = 34.5\ \mu m$, and $d_0 = 5.8\ \mu m$. These parameters yield a theoretical contact angle of 10°.

At static equilibrium, the electrostatic and mechanical torques are coupled through the equation

$$T_m(\theta) = T_e(V,\theta). \tag{7}$$

Points where the curves intersect represent solutions to equation (7). As shown in Fig. 3, there are three types of intersecting points, labeled A, B, and C. For a low equilibrium voltage V_e, the curves will intersect in the region near A. As the voltage increases the intersection moves up the dashed curve. When the voltage exceeds the critical snap-on voltage V_s at point B, the yoke unstably rotates until it contacts the substrate. The yoke is held in the contact position by a voltage much greater than needed for static equilibrium in the region near point C. As a result, the yoke will remain in contact until the voltage falls below the equilibrium release voltage V_r for a given contact angle in the region near C. At this point the voltage will be too low to maintain equilibrium in region C and the yoke will snap back to region A.

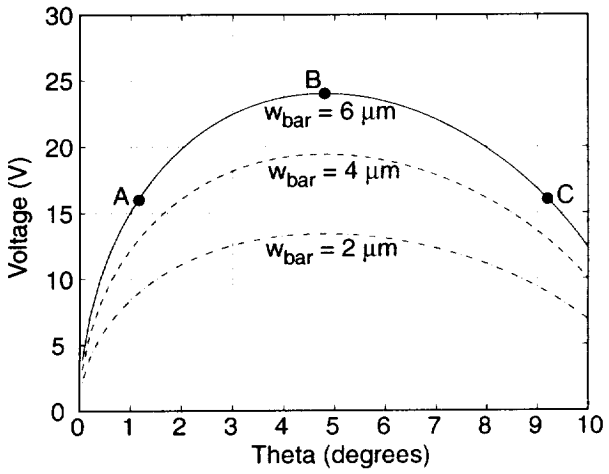

Figure 4: Solutions to equation (8) for various torsion bar widths.

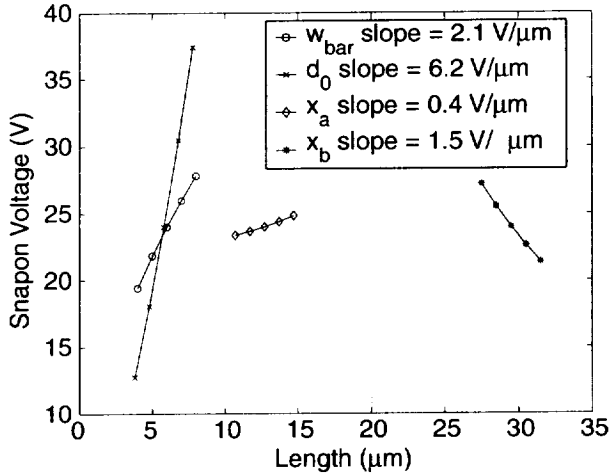

Figure 5: Sensitivity of the snap-on voltage (V_s) to various geometric parameters.

Equation (7) can be used to determine V in terms of θ as follows

$$V = \sqrt{\frac{2\theta^3 KG}{\varepsilon_0 L_{bar} \int_{x_a}^{x_b} \frac{xY(x)}{\rho(x,\theta)^2}\, dx}}. \qquad (8)$$

The above equation is plotted in Fig. 4 for various bar widths w_{bar}, and the points A, B, and C are labeled consistent with Fig. 3. Equation (8) can be used to determine V_e and V_r. At the snap-on voltage, both V_s and θ_s are unknown. However, these values are located at the local maximum. For the dimensions used in Fig. 3 the resulting snap-on voltage and angle of inclination are $V_s = 24\ V$ and $\theta_s = 4.8°$, respectively. For a contact inclination angle of $\theta_r = 10°$, the corresponding release voltage is $V_r = 12\ V$.

Maximized solutions to equation (8) can also be used to study the sensitivity of the snap-on voltage V_s to various geometric parameters. Fig. 5 shows the variation in V_s for four key geometric parameters. This figure shows that the initial plate separation d_0 has the most impact on V_s. Increasing the bar width w_{bar} has nearly the opposite effect as increasing x_b. The parameter x_a has much less effect than x_b, which matches intuition.

2.2 Finite Element Model

In this section, we present results from a detailed mechanical finite element model of the key structural components in conjunction with equation (1). This model more accurately represents the system stiffness, and accounts for the vertical deflection neglected by the analytical model.

The mechanical finite element model consists of the posts, torsion beams, and yoke as shown in Fig. 6. Brick elements are known to significantly over estimate the stiffness of high aspect ratio structures. As a result, the torsion beams and yoke are modeled with shell elements. The mechanical properties of bulk aluminum are used for the post, beam, and yoke. The base of the posts are fixed, and equation (1) is used to compute the pressure distribution for a given voltage and angle of inclination.

The pressure distribution is a function of the orientation of the yoke. As a result there is a highly nonlinear and coupled interaction between the electrostatic and mechanical behavior, which we simulate with a numerical procedure. In this procedure, the voltage is applied in small increments, and the solution iterates between the electrostatic and mechanical solutions until achieving convergence. During the voltage increment that spans the snap-on voltage V_s, the solution for θ increases unstably until the yoke contacts the substrate. Consequently, the mechanical finite element model must account for contact between the edge of the yoke and the substrate. The above procedure was implemented with a program written in the PERL computer language [4], which calls UAI/NASTRAN [5] as needed to solve the finite element equations.

The finite element (FE) and analytical models were used to plot θ versus input voltage in Fig. 7 for $w_{bar} = 4$ and 6 μm. Similar micro-mirrors were fabricated and tested[6], and the measured snap-on voltage V_s of approximately $14V$ for $w_{bar} = 6\ \mu m$ is also included. The FE results show that the contact angle is less than 10° due to vertical deflection of the torsion beams. The FE results over-predict the measured snap-on voltage, and the analytical results over-predict the FE results. The first discrepancy may be due to a mismatch between the model and experimental initial offset d_0, which is difficult to measure experimentally, and the finite element model may be too coarse. The second discrepancy is due to the vertical deflection, which is not included in the analytical model. Despite these discrepancies, the

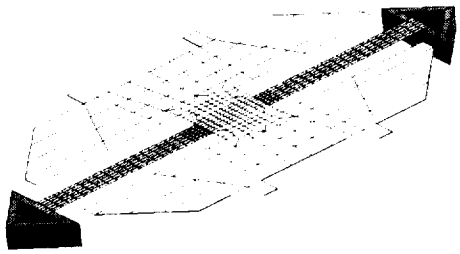

Figure 6: Finite element mesh of the yoke, torsion bar, and post assembly.

analytical and finite element models predict the same trends, which validates the slopes presented in Fig. 5.

3 THERMAL SIMULATION

While the fabrication temperatures of the micro-mirrors are $20°C$ or above, the operating temperature is 30K. The resulting change in temperature of -263K, coupled with the Coefficient of Thermal Expansion (CTE) mismatch between the aluminum structure and silicon substrate results in significant internal stresses.

The average Young's moduli of aluminum and silicon from $293K$ to $30K$ are approximately $71.7 \times 10^9\ GPa$ and $175 \times 10^9\ GPa$, respectively. While the thickness of the torsion bars are approximately $0.3\ \mu m$, the substrate thickness is on the order of $600\ \mu m$. Hence, the substrate will contract independent of the supported structure. The resulting net thermally induced relative displacement between the two posts is

$$\delta_{net} = (\alpha_{al} - \alpha_{si}) L_{total} \Delta T \qquad (9)$$

where α is the CTE averaged over the specified temperature range, and L_{total} is the total structure length. In this case $\alpha_{al} = 19.3e{-}6\ ppm/K$, $\alpha_{si} = 0.82e{-}6\ ppm/K$, and $L_{total} = 135\ \mu m$. The resulting relative displacement is $\delta_{net} = 0.656\ \mu m$.

The above lateral displacement results in an out-of-plane bending moment on the torsion bars and non-linear geometric behavior due to the offset between the yoke and torsion beam mid-planes. As a result, δ_{net} was applied to the base of one post in the finite element model while the other post remained fixed, and a non-linear geometry finite element analysis was completed using UAI/NASTRAN. The solution predicts a peak Von Mises stress near the ends of the torsion bars of approximately 445 MPa due to the combined axial tension and bending. This value exceeds the room temperature yield strength of aluminum by 35%. However, fabricated micro-mirrors have survived cryogenic testing, indicating that local yielding in the torsion bars is likely.

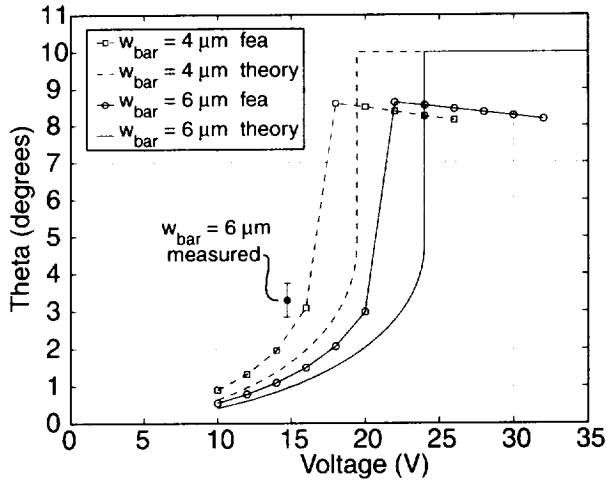

Figure 7: Voltage versus yoke inclination for two different torsion bar widths.

4 CONCLUSION

Analytical and numerical models of aluminum micro-mirrors subjected to cryogenic temperatures were presented. While the model predictions are in coarse agreement with measured values, the analytical and numerical models predict similar trends due to geometric variations. The differences in model and measured data fall within expected shortcomings due to modeling assumptions, and can be corrected with further model development and correlation. In particular the analytical model can be extended to account for the vertical deflection. The finite element mesh can be refined and the initial plate separation d_0 can be adjusted to correlate with experimental results. In future work, the thermal and electro-mechanical models can be merged to predict the response at cryogenic temperatures.

REFERENCES

[1] M.A. Michalicek, D.E. Sene, and V.M. Bright, "Advanced Modeling of Micromirror Devices," Int. Conf. on Integrated Micro/Nanotech. for Space Apps., 214-229, 1995.

[2] J.D. Jackson, "Classical Electrodynamics, Third Edition," John Wiley & Sons, 1999.

[3] W.C. Young, "Roark's Formulas for Stress and Strain, Sixth Edition," McGraw-Hill, 1989.

[4] L. Wall, T. Christiansen, and R.L. Schwartz, "Programming Perl, Second Edition," O'Reilly and Associates, 1996.

[5] Universal Analytics, Inc., "UAI/NASTRAN User's Guide for Version 20.0," Torrance, CA, 1997.

[6] S.B. Dutta, D.B. Mott, C.A. Allen, J.L. Kuhn, J.W. MacKenty, and R.L. Smith, "Development of a 3x3 Array of Individually Addressable Micro-Mirrors for Space Applications ," Int. Conf. on Integrated Nano/Microtech. for Space Apps., 2000.